JOINT EUROPEAN TORUS

JET–P(89)15

G. Braithwaite, N. Gottardi, G. Magyar, J.O'Rourke, J. Ryan, D. Véron
and JET Team

JET Polari–interferometer

"This document contains JET information in a form not yet suitable for publication. The report has been prepared primarily for discussion and information within the JET Project and the Associations. It must not be quoted in publications or in Abstract Journals. External distribution requires approval from the Publications Officer, JET Joint Undertaking, Abingdon, Oxon, OX14 3EA, UK".

"Enquiries about Copyright and reproduction should be addressed to the Publications Officer, EFDA, Culham Science Centre, Abingdon, Oxon, OX14 3DB, UK."

The contents of this preprint and all other JET EFDA Preprints and Conference Papers are available to view online free at www.iop.org/Jet. This site has full search facilities and e-mail alert options. The diagrams contained within the PDFs on this site are hyperlinked from the year 1996 onwards.

JET Polari–interferometer

G. Braithwaite, N. Gottardi, G. Magyar, J.O'Rourke, J. Ryan, D. Véron[1]
and JET Team*

JET-Joint Undertaking, Culham Science Centre, OX14 3DB, Abingdon, UK

[1]Centre d'Etudes de Limeil Valeton, Boite Postale 27, 9410 Villeneuve Street, Georges, France
** See Appendix 1*

Preprint of Paper to be submitted for publication in
Review of Scientific Instruments

THE JET POLARI-INTERFEROMETER

G. Braithwaite, N. Gottardi, G. Magyar, J. O'Rourke, J. Ryan and D. Véron*

JET Joint Undertaking, Abingdon, Oxon OX14 3EA, UK
* Centre d'Etudes de Limeil Valenton, Boite Postale 27,
94190 Villeneuve St Georges, FRANCE

ABSTRACT

A multichannel far infrared interferometer used on the Joint European Torus (JET) is described. The light source is a 195 μm DCN laser. The instrument is of the Mach-Zehnder type, with a heterodyne detection system. The modulation frequency (100 kHz) is produced by diffraction from a rotating grating. There are 6 vertical and 2 oblique channels. The latter rely on retro-reflection from mirrors mounted on the vessel wall. Their vibration is compensated by a second wavelength interferometer at 118.8 μm. The various subsystems are described, with emphasis on features necessitated by (a) large path lengths; (b) remote handling requirements; (c) fluctuations in atmospheric humidity, and (d) unmanned automatic operation. Typical measurements, along with real-time and off-line data analysis, are presented. The phase-shift measurement is made with an accuracy of $\frac{1}{20}$ of a fringe, corresponding to a line integrated electron density of $5\times10^{17}\,m^{-2}$. Comparison with other electron density diagnostics are shown.

The introduction of additional optics allows measurements of the Faraday effect and a determination of the poloidal magnetic field distribution. The signal processing and data analysis are described. Errors introduced by the calibration procedure, birefringence of the probing beams, toroidal field pick-up, the flux geometry, and the density profile are considered. The Faraday angle is measured with an accuracy of 5%, and a time resolution of 1-10 m s. The poloidal magnetic field is deduced with an accuracy of $\pm$15%.

I. INTRODUCTION

Laser interferometry for measuring electron density has become a standard diagnostic on most tokamaks[1]. As the laser beams are usually polarized, the Faraday-effect may provide a second piece of information—on the poloidal magnetic field distribution in the plasma—assuming the density is measured simultaneously. Such polarimetry is now also used for tokamak diagnostics[2].

A multichannel far infrared (FIR) interferometer has been used on JET routinely since 1984[3]. In 1987 it was supplemented by polarimetry[4]. In the present paper we intend to describe the system in its final form on JET. A schematic view of the vertical probing part is shown in Fig. 1a and of the lateral probing in Fig. 1b. For completeness all 10 original channels are shown although due to machine modifications channels 7 and 9 were occluded. For clarity the added optics of polarimetry will be shown separately in Fig.8.

The main parameters of the system are: measuring range of line density from $\sim 5\times10^{17}$ to $10^{21}\,m^{-2}$, time resolution $\sim10^{-4}$ s, spatial resolution $\sim$20 cm, Faraday rotation angle from 0° to $\sim$ 45°, number of samples per channel per shot 4 kbytes.

As this diagnostic will be used during the D-T phase of JET, all the active components (lasers, detectors, electronics) are outside the Torus Hall, behind the 3 m thick biological shield. The optical link with the Torus Hall is established via the basement.

The interferometer is of the type first reported by Véron[5]. The special engineering features of JET, like large distances, large plasma, remote handling etc. created many new problems and solutions worth reporting.

We shall first discuss the major components of the interferometer system: lasers, optics, mechanics, compensating interferometer, data acquisition and analysis. Then in the second part, on polarimetry, the additional optics, the signal processing, calibration, and data analysis.

II. INTERFEROMETER

II.1 Lasers

The basic source of radiation is a DCN (deuterium cyanide) laser operated at 195 μm. Actually there are two such lasers with a common entry point to the system so that one is always available while the other is being maintained or under repair.

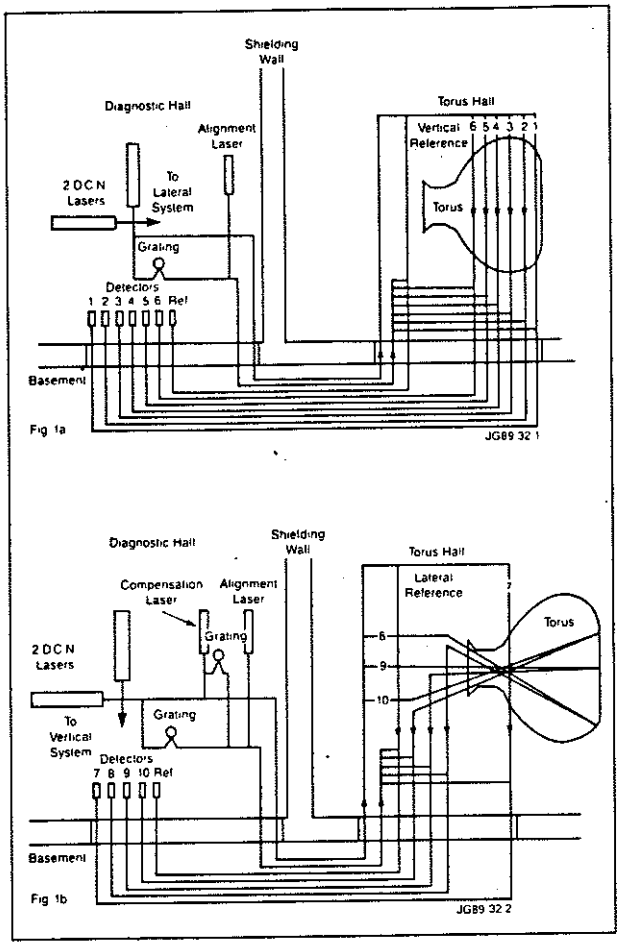

Fig. 1 Schematic view of the FIR Interferometer System
(a) Vertical probing (b) Lateral probing

This wavelength was chosen to avoid refractive effects in the large path through the JET plasma (~4m) and at the same time not to be affected by the mechanical vibrations on the short wavelength side. Power can be as high as 400mW, all lines, 250mW in our single line, but a typical average is ~300mW (~180mW at 195 μm).

As JET operates 16 hours per day, 5 days per week, reliability of the laser is a major requirement. In fact, an initial difficulty was the variable performance of the DCN laser over long periods in comparison with the well-tested HCN laser. This was due to the much more vigorous carbonisation of the laser cavity, requiring frequent maintenance and increased UV radiation wearing out components earlier. Both effects were due to the CD_4 gas component of the supply mixture. The problem was solved by the construction of an automatic control system to reduce the flow of CD_4 to 1-1½ hour per day. This allows the laser to run a He-N_2 discharge between plasma shots (~half an hour) and introduces CD_4 only three minutes before the JET pulse.

Due to diurnal variations of humidity which absorbs the laser radiation, the signal amplitude may vary significantly. For this reason, the microprocessor-based control unit waits for the signal to reach a steady level after the introduction of CD_4 and then checks each channel cyclically and, if necessary, adjusts their amplitude to be between acceptable limits for the data acquisition system. In this way, reliable unmanned operation became possible.

The laser tubes were also redesigned to avoid any weak joints thus prolonging their lifetime. Frequent checks were introduced to antici pate problems of wear and tear, dirt etc. Thus availability of the system has reached ~98%.

The source for the compensating interferometer is a commercial CO_2- laser-pumped CH_3OH laser at 118.8 μm. The pumping power is ~45W, the FIR output is typically ~180mW (without calorimeter correction). To keep this power within acceptable limits (±5%) an automatic cavity length control unit was constructed. The feedback system uses the amplified output of the reference detector and tunes with its aid the output mirror of the alcohol laser via a stepping motor.

II.2 The beam-processing optics

The system is separated into a vertical and a lateral subsystem, for convenience. The laser output is therefore split into two equal parts by a quartz beam-splitter. The transmission is critically dependent on the angle of incidence and there are two mirrors in front of the laser to achieve the correct angle (45°), without moving the whole laser bodily. Then there is a quartz Fabry-Perot etalon at Brewster angle to select the operating wavelength of 195 μm. Both beams are then further split into two: a probing beam and a modulated beam as indicated in Fig. 1. The modulation is at 100kHz by a rotating grating—its 3600 grooves rotated at 28Hz. A half-wave plate rotates the beam-polarization so that it arrives in the correct state at the plasma, ie., parallel to the toroidal field.

For alignment purposes a 20mW He-Ne visible laser (6328 Å) is included. Its output is split into four subsidiary beams by four auxiliary beam splitters/mirrors on a slider which can be interposed to simulate the four DCN beams. This power is sufficient to observe the return beams on the detector. This is facilitated by having all the optical components for the FIR compatible with visible radiation: aluminized mirrors, transparent quartz beam-splitters and windows, and transparent mylar windows are used throughout. The alignment of the components is made with an accuracy of ±1mm.

II.2.2 Beam transfer

The input beams are transferred by free optical propagation using aluminized mirrors to the C-frame (tower) in the Torus Hall. First they are sent down into a duct in the basement and then up through a penetration into the tower. Telescopic arrangements keep the beams down to reasonable size.

On the return path the beams are directed into oversized dielectric waveguides (Pyrex tubes of ~80mm inner diameter). It was found[6] that this form of transmisssion is at least as efficient as the free propagation via mirrors, it preserves the polarization direction and, what is most important for JET conditions, it eases the alignment problem. The total distance between laser and detector is ~80m. The entrance to the waveguides is at

~50m. Once the return beam is within the diameter of the entrance it will automatically reach the detector; thus the alignment needs to satisfy only this condition.

For radiological protection the air in the Torus Hall must be isolated from the air in the basement and the latter from the Diagnostic Hall. For this purpose in each exit or entrance port 50 μm thick mylar windows are used which are radiation resistant, highly transmitting both at 195 μm and 6328 Å and can be made into an air-tight window, withstanding expected pressure differences when the Torus Hall and basement will be under-pressurized during the D-T phase.

II.2.3 Beam steering

The probing beams which arrive in the Torus Hall are split up into individual channels. One part is sent back without going through the plasma and recombined with a portion of the modulated beam to constitute the reference beam. The others are made approximately equal in intensity, focused onto the horizontal midplane of the plasma (beam-waist ~20mm at the e-folding point of the intensity profile) and combined with the corresponding modulated channels afterwards. The input and exit windows to the vacuum chambers are made of z-cut crystal quartz in aluminium-bonded ferrules which enable them to withstand baking temperatures up to 420°C. Clear optical diameters vary between 75 and 120mm; thicknesses chosen to give a safety factor of ~8. JET is usually operated at ~300°C, but some of the windows are at lower temperatures, depending on position. Thus their thickness could not be optimized for maximum transmission. To avoid back-reflection the windows are tilted at ~3° from the normal. The high temperature produces air turbulence above the windows which leads to a 'shimmering' of the alignment beams. The position fluctuation can be as high as ±10mm at the location of the detectors, before focusing. This effect introduces phase fluctuations in the beat signal of the order of $\pi/10$.

II.2.4 Detector optics

After returning via waveguides the beams are focused onto the InSb He-cooled detectors. Provision has been made for a TPX lens and polarizer in front of the detectors, but it was found unnecessary. As the detectors are ~2mm square crystals, strong focusing is necessary from the end of the wave-guide. A quasi-parabolic cone guides the radiation to the crystals and HDPE plus carbon-paper filters exclude radiation below 30 μm.

The overall efficiency of the system, ie. (power arriving at the detectors)/(laser output power) is ~2%.

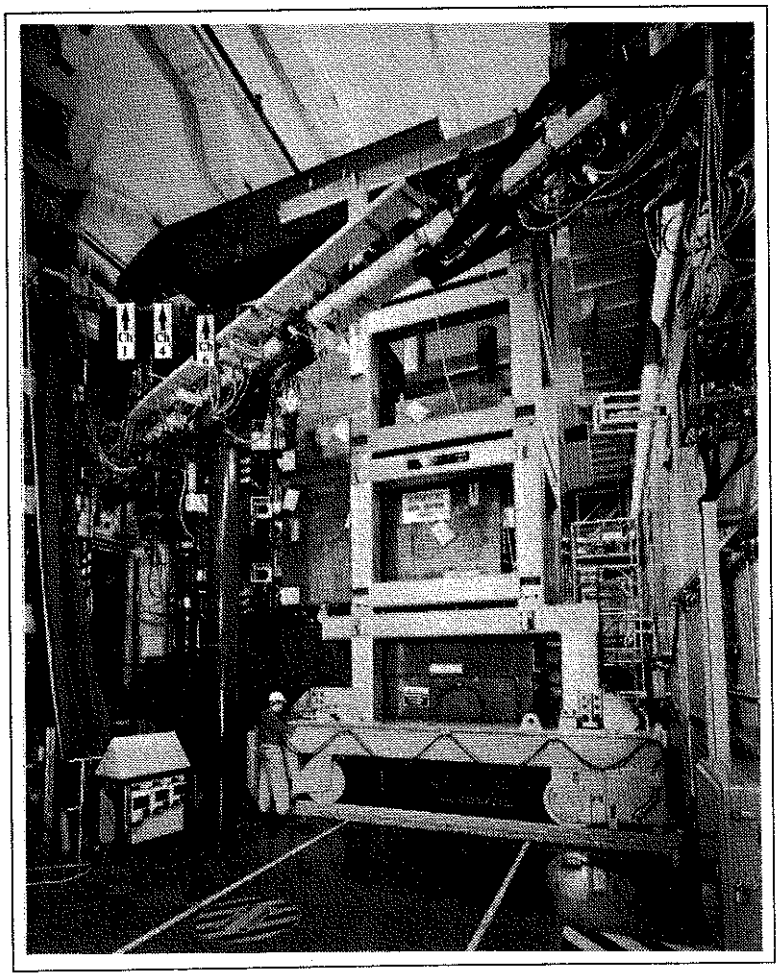

Fig.2 Interferometer C-frame (tower) in the withdrawn position. (Fast transfer system on a column, in front).

II.3 Mechanics

A massive granite table ensures the stability of the beam-processing optics. An air-tight cover keeps out dust and humidity.

The beam transfer optics in the basement are attached to a duct, 17 m long, 1.2×1.2 m cross-section, made of resinated fibre. It is also made air tight and continuously supplied with pressurized dry air, like the rest of the system.

The optics in the Torus Hall is situated in a large C-frame (tower), independent from the machine. The tower rests on a motorised carriage movable on rails so that it can be withdrawn for machine access. Fig. 2 shows the tower in such a position. The tower can be re-positioned with an accuracy better than 100 μm. To suppress mechanical coupling to time varying B fields the optical components are attached inside of resinated fibre boxes: an upper and lower boom for the vertical system and a rectangular box for the lateral system. The tower weighs ~52 tons and is supported on massive springs: this was designed to reduce the mechanical vibrations to ~10 μm at the tip of the boom which is 9 m long. Fig. 3 shows a blown-up trace of the inner-most channel for pulse No. 3013 which demonstrates that, indeed, the noise amplitude of the 195 μm signal is of the order of $\frac{1}{20}$ of a fringe, corresponding to a minimum measurable line density of $5\times10^{17}\,m^{-2}$. The modulation is a characteristic of the ±1 bit excursion of digital output. This vibrational behaviour made the compensating interferometer unnecessary for the vertical system. In fact, several mechanical sensors are attached to the tower in order to measure the movements of the JET machine in various directions.

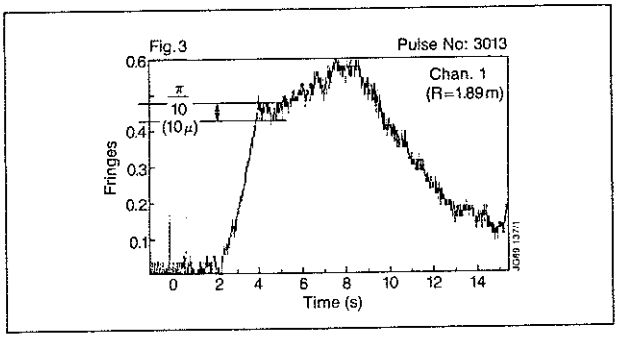

Fig. 3 Noise level on the line integrated density of channel 1.

All the optical components on the tower are remotely alignable. The usual X-Y motions by screws are provided using two reversible pneumatic stepping motors for each mount. The motors are commanded from an electro-mechanical switch via solenoid air-valves. For purposes of orientation, small light bulbs can be lit on the component to be moved. An adjustable observation telescope in the Diagnostic Hall can be inserted in any of the outgoing and incoming beam-paths. Retractable field lenses in the duct help focusing over the large distance involved.

Initially the system needed occasional re-alignment as the components settled and also due to the Torus Hall slowly sinking with respect to the Diagnostic Hall. Recently, however, the system has operated between two major shutdowns ie. over a year, without the need for re-alignment.

The 195 μm radiation is very sensitive to atmospheric humidity. Therefore the input-output entrances of the boxes are sealed with mylar windows. The dry air comes from a compressor and filter array. A relative humidity of 0.1 % or less is required due to the large distances. The main difficulty arises from pressure differences, due to a complicated ventilation system between Diagnostic Hall and basement, which draw in humid air even through tiny leaks. The problem was eased when isolating mylar windows were interposed at the building interfaces. Thus each channel passes through 6 isolating windows.

All the components in the Torus Hall are radiation resistant to the maximum level forseen during the D-T phase of JET eg. special radiation- hardened diodes are used to prevent cross-talk in the matrix of the solenoid-pneumatic control. The possible detrimental effect of high magnetic field is avoided by the use of pneumatics and non-metallic support of optical components near the machine. The booms and the optical components inside have been designed for remote handling such that a repair and/or replacement could be carried out in the Hot Cell.

II.4 Compensating interferometer

The JET plasma is D-shaped. Hence it is important to have views in addition to the vertical lines of sight if a proper density profile is required. For this reason the lateral system was designed with three channels: one horizontal, one at 19° above it and the third one at 32° below. These must use mirrors attached to the inner wall of the vacuum chamber and make a double path through the plasma. This introduced sensitivity to vessel movement and required a compensating interferometer which would measure the phase shift due to mechanical displacement. This displacement is especially large during the change of the toroidal field: the vessel wall bends so much that a plane or spherical mirror would send the return beam completely off the waveguide resulting in signal loss. As the angular movement is one-dimensional, use of roof-top mirrors solved the problem. (Corner cubes are not applicable because of the separate input and output windows).

At the outset the 3.39 μm wavelength of a He-Ne laser was used as it is sensitive to the mechanical vibration alone. It can pass the same optics as the FIR beam. However the beams returning from the internal mirrors became fainter due to surface damage and mainly due to carbonisation. The latter is more detrimental the shorter the wavelength.

The same fate befell the visible alignment beams: the initial 35% reflectivity of the Nickel roof mirrors deteriorated to 0.003 %, hence the alignment possibility was completely lost. Due to the small size of the beam, its short wavelength and the lack of waveguide action

at 3.39 μm, the alignment was very critical and needed frequent adjustment. Without the visible alignment the weak infrared signal was adjusted by 'trial and error' to keep a sufficiently high beat signal. In this way the usefulness of the lateral channels was demonstrated, but after more extensive carbonisation the 3.39 μm signals were completely lost.

It was decided to replace this wavelength with a much longer one, sharing the advantages of the 195 μm: insensitivity to carbonisation and ability to use the waveguide. The 118.8 μm radiation of the alcohol laser (see Ch.II.1) was chosen. As the existing optics must be used, some inevitable losses had to be accepted: the beamsplitters have lower reflectivity, absorption in 10mm of quartz is ~40%, in kapton ~25%, in humid air it is by a factor 3.3 more than at 195 μm.

To avoid losses in numerous kapton windows, which were used initially, it was found that 50 μm thick mylar reduced this loss to ~5%, the same as for 195 μm. It was tested and found radiation resistant so it replaces kapton everywhere.

Lack of space necessitated the use of the same In Sb detectors; their sensitivity decreases by more than an order of magnitude at 118.8 μm. Nevertheless the available laser power gives usable signals. Optical separation of the two wavelengths is not easy, without significant modification of the system. It was decided to separate them electronically by modulating them at greatly differing frequencies—the 195 μm at 100 kHz as before and the 118.8 μm at 5 kHz (by a rotating grating)—and then filtering. The fringe counting electronics had to be modified to attenuate strongly the unwanted frequency, without undue phase shift and to lock the fractional fringe counter to 5 kHz (see section II.5). Spurious 5 kHz modulations had to be eliminated.

It should be noted that the 5 kHz modulation introduces a fundamental limitation of 5 fringes m s (of the 118.8 μm signal) on the maximum fringing rate which can be measured. This corresponds to changes in the line-integrated electron density of the order of $10^{23}\,m^{-2}s^{-1}$, which is adequate except in certain pellet injection experiments.

Fig. 4 shows the 195 μm and 118.8 μm signals of channel 10 as they both respond to mirror motion induced by the fall of the toroidal field and the third signal, representing the net density trace after correction for mechanical motion.

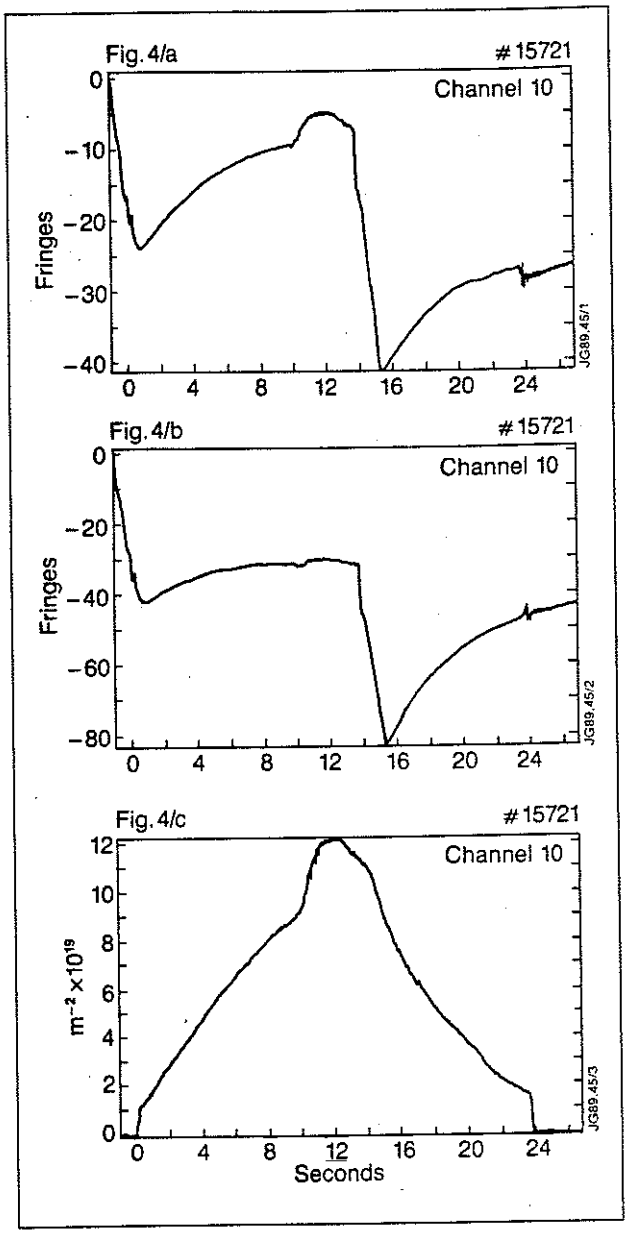

Fig. 4 Typical result of the compensating interferometer (Channel 10):
(a) Phase shift versus time (195 μm interferometer);
(b) Phase shift versus time (118.8 μm interferometer);
(c) Net line integrated density versus time.

II.5 Data acquisition and analysis

The detectors are Indium Antimonide crystals, with six of them situated in a common cryostat for liquid Helium. There are two cryostats for the interferometers and one for the polarimeter. The system is kept cooled down all year round, except major shutdowns. The holding time is 10 days for one and two weeks for the other two cryostats. A preamplifier with a gain of 100 is directly connected to the crystal and then the output goes to fringe digitizing CAMAC units. The fringe number is obtained by recording the difference between the number of zero crossings experienced by the reference channel signal and the probing channel signals. As this number is low on JET—of the order of 10—fractional fringe counting is necessary. It is done by multiplying the modulation frequencies electronically by 32 and carrying out a similar zero-crossing detection. This limits the accuracy to $\frac{1}{32}$ of a fringe which is better than the mechanical limit of $\frac{1}{20}$ mentioned earlier. Supporting evidence is that the sawtooth modulation of the electron density which is at the 1% level is detected on the central channels.

Fig. 5 shows a typical direct output of the system: the line densities in the six vertical channels. Also shown is the total number of elec trons calculated and the ratio of the line-averaged to volume-averaged densities.

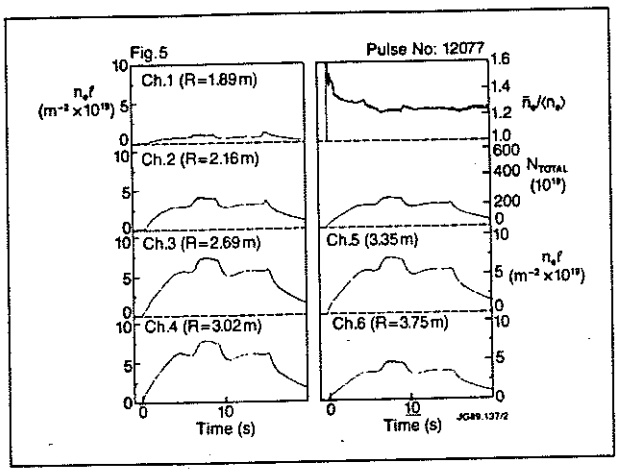

Fig. 5 Typical output from the interferometer diagnostic.

The line-integrated density measured by the FIR interferometer is required not only for diagnostic purposes, but also in real-time for machine control. The two real-time applications are the Density Feedback and the Plasma Fault Protection System[7]. Although the fringe counters convert the line-integrated density to an analogue real- time signal, this in itself is not sufficient since the signal must also be validated as being free of fringe jumps. This is accomplished according to three criteria: (a) agreement (within a predetermined tolerance) between different FIR channels and/or the single chord 2mm interferometer;[8] (b) sufficient signal amplitude; (c) no detected fringe jumps. This leads to 'high confidence' level. In certain pellet-injection scenarios criterion (d) cannot be fulfilled. For this purpose the bremsstrahlung radiation monitor is included which is not a phase-dependent measurement. It does not give absolute values of density but is proportional to

$$Z_{eff}\, n_e^2 \frac{e^{-h\nu/kT}}{T^{1/2}} \qquad \ldots (1)$$

where Z_{eff} is the effective ion charge, n_e is the electron density, ν is the frequency of the detected light and T is the electron temperature. Hence, since the temperature dependence is weak at the frequency considered ($h\nu \ll KT$) and if one assumes that the change in impurity content is negligible during the time interval considered, one can compute the change in n_e from the change in the Visible Bremsstrahlung signal. It is continuously compared with the interferometer and serves to renormalize the density signal after a fringe loss. Although this is regarded as 'low confidence', it still allows the plasma operation to proceed.

To obtain the density distribution, there are several Abel-inversion procedures in JET which give results all in very good agreement. The methods specifically developed for this diagnostic apply inversion procedures which introduce smoothing of data from the total number of chords (vertical and oblique) in a consistent manner.

One method[9], developed previously under contract for JET, does this by applying auxiliary conditions on the Laplacian of the source function. This tends to bias the inverted profiles toward the 0th order cylindrical Bessel function.

The approach we are presenting here is to transform the data from the actual chords to that of a 'virtual' set of chords, chosen for its symmetry. The transformed data can then be smoothed by any conventional smoothing routine and then inverted.

For n chords of data we define n pixels, whose boundaries are the flux surfaces tangent to the chords. We calculate the path length for each chord through each pixel, and store the results in an $n \times n$ matrix, N. Similarly, we calculate two $n \times n$ matrices, A and B, for two sets of 'virtual' chords, each of which is an entirely vertical array of chords tangent to the same flux surfaces as the actual chords (for each flux surface there are two vertical tangent chords, one on either side of the magnetic axis).

The $n \times 1$ data matrix can then be transformed by applying the transform matrices AN^{-1} and BN^{-1} to generate $2n$ 'virtual' data points, which are a continuous function of the major radius.

A new set of k uniformly spaced pixels is defined, with a corresponding path-length matrix K and k data points obtained by smoothing of the $2n$ 'virtual' data points. Finally, the local density is obtained by applying K^{-1} to these data.

Fig. 6 shows the time evolution of inverted chordal data for a typical JET plasma.

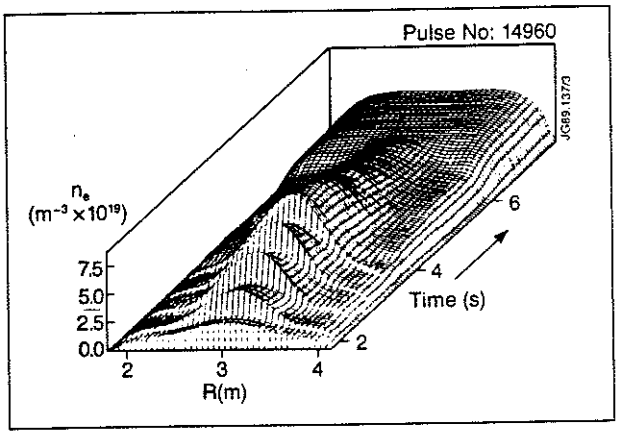

Fig. 6 Time evolution of the density profile during a pellet fuelled discharge.

There are four diagnostic systems on JET which measure electron density: the FIR interferometer, the single-channel microwave interferometer, the reflectometer and the LIDAR Thomson Scattering. Comparison of their equivalent outputs shows better than 5% agreement with the interferometer. Fig. 7a compares the line-integrated density of channel 4, at major radius, $R = 3.02$ m and that of the microwave interferometer at $R = 3.1$ m. Fig. 7b compares the density profile in shot 3886 obtained by the FIR interferometer and the single channel reflectometer. Finally, Fig. 7c compares the density profile in shot 12237 obtained simultaneously by the interferometer and the LIDAR Thomson Scattering. It

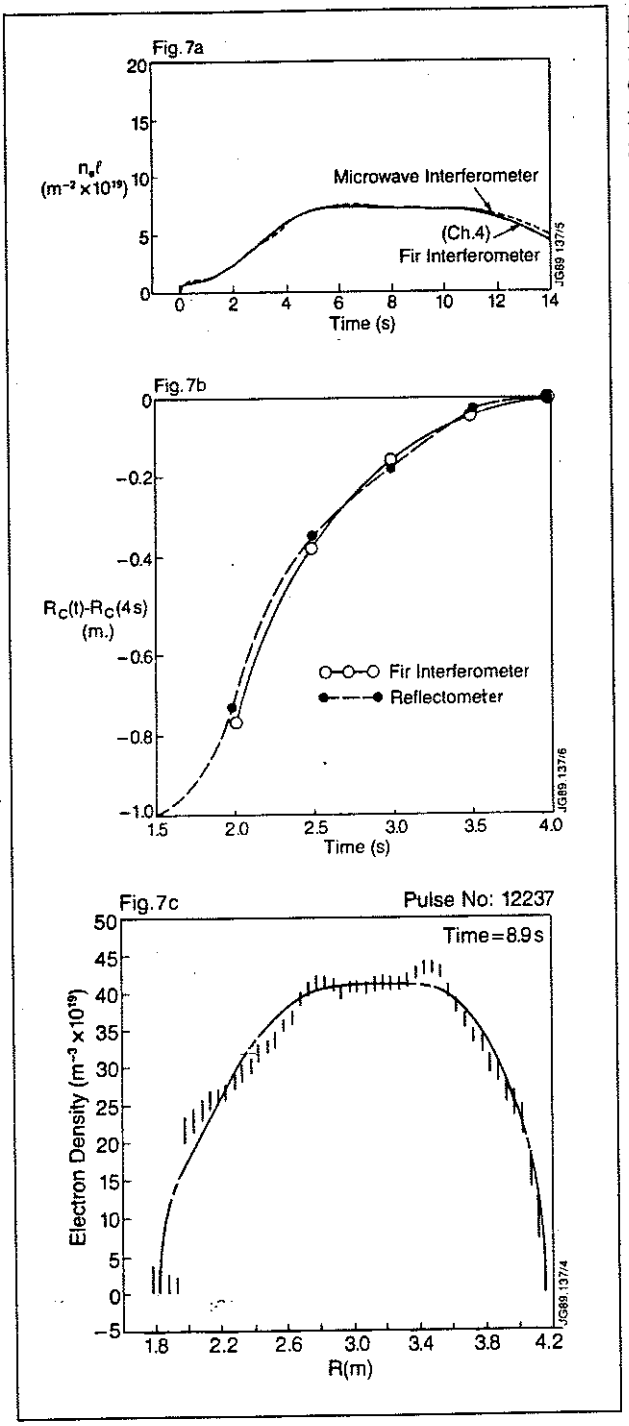

Fig.7 Comparison of results from different density diagnostics
(a) Channel 4 of the FIR Interferometer (KG1) and the single-channel microwave interferometer (KG2);
(b) Density profile by KG1 and by the prototype reflectometer;
(c) Simultaneous density profile by KG1 and the Thomson-scattering LIDAR system.

should be noted that in the cases 7b and 7c the profiles were calibrated at one point against the interferometer.

III POLARIMETER

III.1 Optics

The six vertical channels of the JET far-infrared multi-channel interferometer have been modified to also make polarimetric measurements (Faraday rotation). The configuration is essentially as described in[10] and consists of a simultaneous measurement of the probing beam intensity along two orthogonal directions of polarization.

In JET, however, the half-wave plates which are used for calibrating the system are located before the input of the beams into the torus (rather than at the exits). Also, the recombination of the probing and refer ence beams and the separation of the unrotated and rotated components is done in 2 stages, using a polarization-independent beam splitter for the former and a tungsten wire grid for the latter. (See Fig. 8).

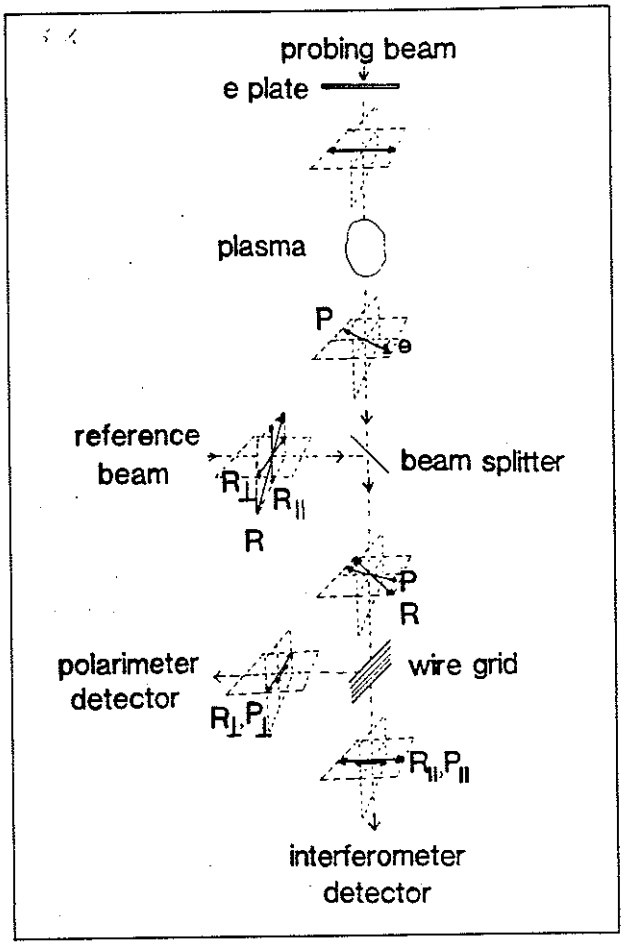

Fig.8 Schematic view of the polarimeter.

III.2 Signal Processing and Calibration

The 'interferometer' signal is proportional to $\cos\theta$, where θ is the angle of Faraday rotation, while the 'polarimeter' signal is proportional to $\sin\theta$. The first is squared to produce a DC signal proportional to $\cos^2\theta$, the second is multiplied by the first in a phase-sensitive detector to produce a DC signal proportional to $\sin\theta\cos\theta$. The two DC signals are digitized, and their ratio used to determine $\tan\theta$ (see Fig. 9).

This method of measurement requires a calibration, which is performed by rotating quartz half-wave plates (located at the point of entry of the beams into the torus)

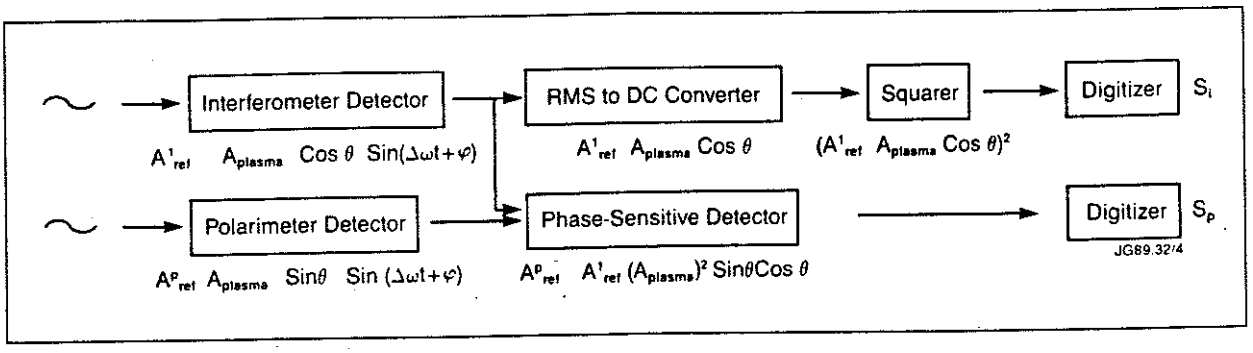

Fig.9 Schematic of polarimeter signal processing.

to produce a rotation of the beam polarization in steps of 0.4° (Fig. 10).

The measurement of the Faraday rotation angle is made with an error $<5\%$, and a sensitivity of $\sim 1\%$.

The time resolution is 1-10ms., determined by the integration time of the electronics. The lower limit on the time resolution is set by the 100kHz modulation frequency of the polari-interferometer.

The time evolution of the measured Faraday angles for a 4MA ohmic discharge is shown in Fig. 11.

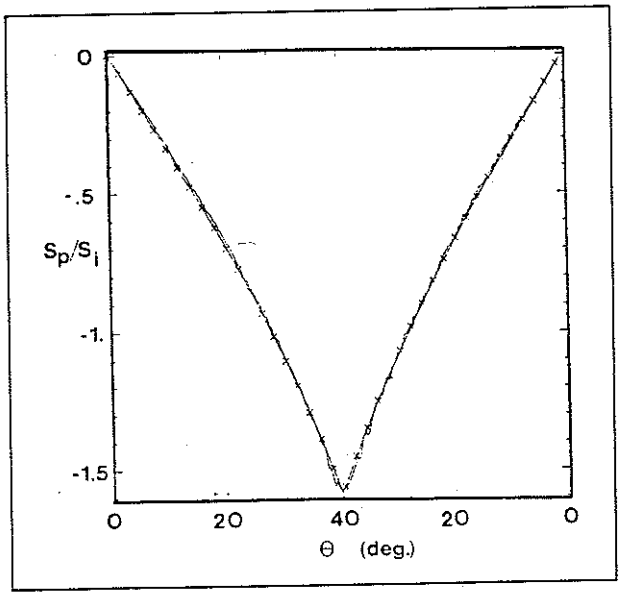

Fig. 10 Ratio of the polarimeter signal to the interferometer signal versus rotation angle during a calibration of channel 3 ($R = 2.7$m). Also shown is the fitted curve (crosses) $S_p/S_i = c \tan\theta$ where c is the calibration factor.

III.3 Data Analysis and Results

The Faraday rotation angle is proportional to $\int n_e B_{\parallel} d\ell$, where n_e is the electronic density and $B_{\parallel}$ is the magnetic field along the probing chord. This implies that polarimetric measurements must be used in conjunction with other diagnostics to infer the poloidal field distribution. In particular, the non-circularity of JET cross- sections means that the poloidal field enters into the Abel inversion of the chord-integrated data both as a parameter (determining the shape of the flux surfaces) and as the

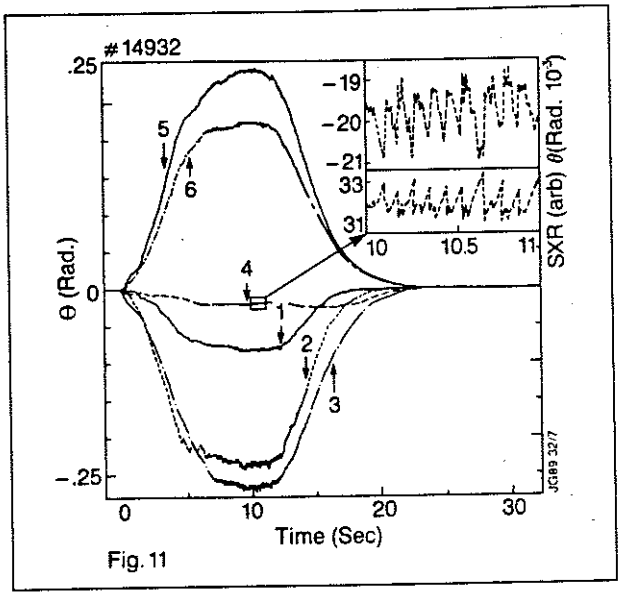

Fig. 11 Faraday angle versus time during a 4MA ohmic discharge. The inset shows the sawtooth modulations on the central channel ($R = 3.02$m), and on the Soft X-ray intensity.

unknown to be determined. In the results presented here the flux geometry is determined from magnetic measurements at the plasma boundary via an equilibrium identification code, IDENTC[11]. The poloidal field distribution is then determined by a generalized Abel inversion in this geometry, Fig. 12. The electron density profiles are obtained from the interferometric data or from the LIDAR diagnostic[12]. The Abel Inversion is made in 2 steps. The discharge cross-section is divided into six nested elements, determined by the flux surfaces of tangency of the six polarimetric chords. A first calculation of the poloidal field distribution is made in this geometry, and used to calculate the expected angle of Faraday rotation on six vertical 'virtual' chords, tangent to the same flux surfaces, but on the opposite side of the magnetic axis to the corresponding real chords. A Chebyshev polynomial is fitted to the complete set of Faraday rotation angles (real, virtual + zero points at the plasma boundary) and the second Abel inversion is performed on this smoothed data. This method ensures that the smoothed data conforms both to the data and to the transformation properties implied by the flux geometry. Fig. 13 shows the results of such a calculation.

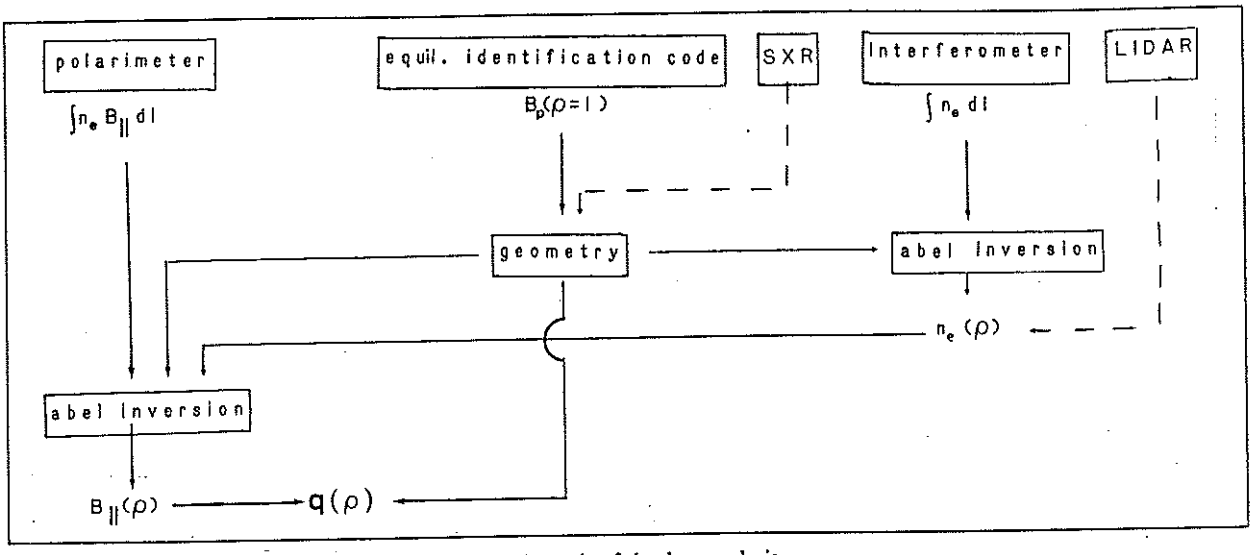

Fig. 12 Schematic of the data analysis.

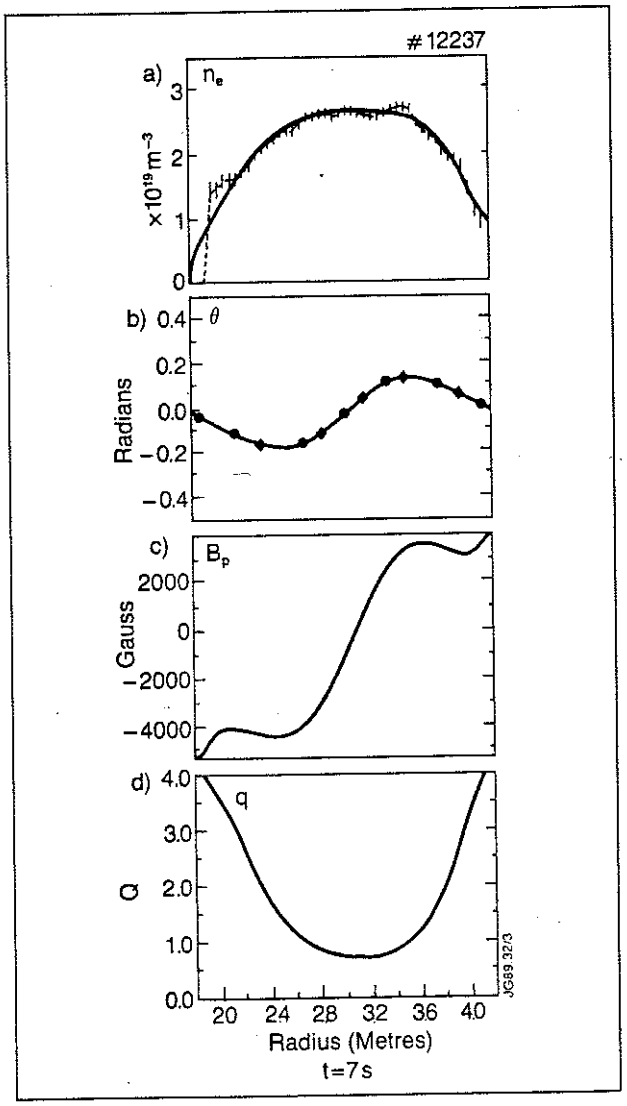

Fig. 13 An example of the determination of the q-profile.
(a) The Abel-inverted density profile compared with the LIDAR profile.
(b) The measured Faraday angles (circles), the mirrored angles (diamonds), and the fitted angles (solid line).
(c) The deduced poloidal field.
(d) The safety factor profile $q \equiv \frac{d\phi}{d\psi}$ where ϕ is the toroidal flux and ψ the poloidal flux.

III.4 Sources of Error

A number of effects contribute to the error in the measurement of the poloidal field distribution. Uncertainty in the calibration, secondary effects due to birefringence and toroidal field pick-up, uncertainty in the geometry of the flux surfaces, and sparseness of the data, and uncertainty in the electron density profile lead to an error in B_p of about $\pm 15\%$. Much of this error is systematic and changes in the B_p-profile can be measured with considerably better accuracy.

III.4.1 Calibration

Calibrations as shown in Fig. 10 are reproducible to better than 5%. Nevertheless, drifts in the alignment of the system make it necessary to repeat the calibration procedure frequently (at least once a day).

III.4.2 Secondary effects

Birefringence introduces an elliptic polarization of the probing beam, $\epsilon \equiv b/a$, which appears primarily as a phase shift $\Delta\psi$, of the polarimeter signal with respect to the interferometer signal:

$$\Delta\psi = \tan^{-1}\left(\frac{\epsilon}{\tan\theta}\right) + \tan^{-1}(\epsilon \tan\theta) \quad \ldots (2)$$

Plasma-induced birefringence does not contribute significantly to measurement errors at the relatively low toroidal fields on JET. Beam refraction can cause further birefringence, however, by changing the angle of incidence into the dielectric wave guides used on the return portion of the beam path[6]. In order to make an estimate of the error introduced by birefringence, we have measured the Faraday angle with the interferometer signal shifted by 90°, as well as in the usual way with the interferometer signal unshifted, as in Fig. 9. (In the absence of any birefringence, the measurement made with the shifted interferometer signal should give no output on the phase sensitive detector (PSD) since the interferometer and polarimeter signals are out of phase). The ratio of the shifted and unshifted PSD outputs is

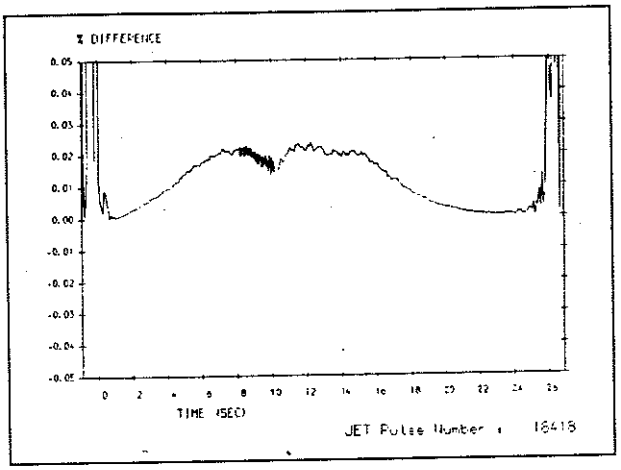

Fig. 14 Relative difference between Faraday rotation measurements with and without birefringence corrections.

proportional to tan ($\Delta\psi$) and is a direct measurement of birefringence. Fig. 14 shows the relative change in the deduced Faraday angle when the above measurement of bire fringence is incorporated, showing excellent agreement between the two. Electronics are presently being developed to monitor birefringence on all 6 channels.

As a further verification that imperfections in the optical components do not lead to significant deviations from ideal behaviour at large rotation angles, one can measure the plasma-induced birefringence along the central chord when the input polarization is set to 45° with respect to the toroidal field. In this limit the change in phase between the 'polarimeter' and 'interferometer' signals should be:

$$\Delta\psi = 1.7\times10^{-22} B_T^2 \int n_e \, d\ell \qquad \ldots (3)$$

This can be compared with the interferometric measurement (Fig. 15). Although the measurement is noisy, being at the limit of the resolution of the phase digitizer the agreement is good.

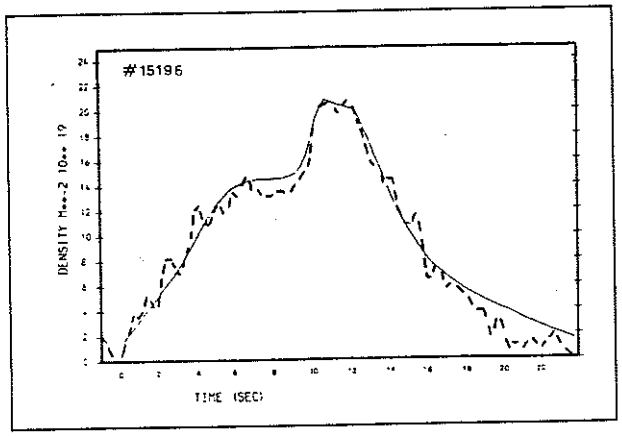

Fig. 15 Measurement of the line-integral density on channel 4 ($R = 3.02$ m).
solid line —interferometric measurement.
dashed line—birefringence measurement.

Finally, due to deviation of the probing chords from verticality, pick-up from the toroidal magnetic field could be an important source of error (~7%). Since both the toroidal magnetic field and electron density must be present in order for the effect to be present, the only way to estimate its importance directly is to produce identical dis charges with the magnetic field reversed. The JET programme has not yet been able to accommodate this experiment. A less direct method of estimating this effect is to compare the Faraday angle on a chord passing close to the magnetic axis with the value calculated from the equilibrium magnetic field and geometry. At this position the Faraday angle is insensitive to details of the poloidal field distribution and close to 0 unless the toroidal field is causing an additional Faraday rotation. The error due to the combined effect of the toroidal field pick up and uncertainties in the flux surface geometry in this case is estimated to be ~0.007 rad or ~1% of the maximum angle of rotation.

III.4.3 Geometry

Since the Faraday rotation measurement is a weighted line integral of B_p, errors in the assumed path lengths lead directly to errors in B_p. In particular, for a set of vertical probing chords, the inferred value of B_p near the plasma centre is approximately proportional to the inverse of the assumed elongation of the flux surfaces at the magnetic axis, κ_0. The elongation of the central flux surface in the equilibrium reconstruction is systematically greater (5-10%) than the elongation of the SXR iso-emissivity surfaces[13]. If the latter are taken to represent the true elongation of the flux surfaces, a higher value of B_p is deduced.

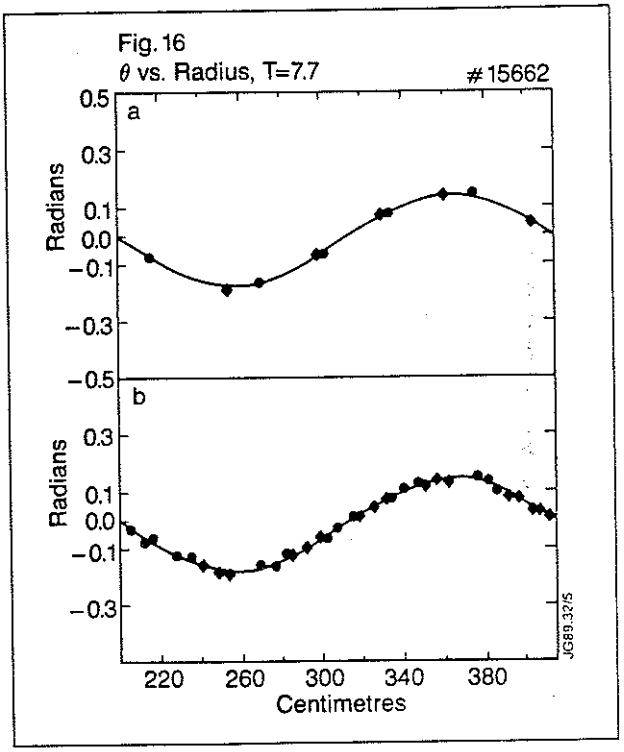

Fig. 16 Faraday angles in a discharge which was displaced across the lines of sight.
(a) data from a single time slice
(b) superposition of 3 time slices to increase the spatial resolution. The fitted angles are nearly identical.

Horizontal displacements of the plasma column experiments have been performed to increase the spatial resolution of the system by super imposing successive time slices. See Fig. 16. The results do not indicate any significant change to the fitted curve with this increased spatial resolution.

III.4.4 Density Profile

Fig. 7c shows a comparison of the electron density profile obtained by Abel inversion of the interferometer data with that from LIDAR-Thomson scattering. The very good agreement between these independent diagnos tics implies that the error introduced by the density profile into the measurement of the poloidal field is $\leq 10\%$.

REFERENCES

[1] D. Véron in 'Infrared and Millimeter Waves', vol.11, ch.2. (Ed. K J Button), Academic Press, New York, pp.67-135(1979).

[2] H. Soltwisch and Equipe TFR, Infrared Physics **21**, 287(1981).

[3] G. Braithwaite, A. Bulliard, J. L. Bruneau, G. Magyar, J. O'Rourke et al., JET Report JET-IR(85)08, (1985).

[4] J. O'Rourke, J. Blum, J. G. Cordey, A. Edwards, N. Gottardi et al., Proc. 15th European Conf. Contr. Fusion & Plasma Phys., Dubrovnik, Yugoslavia (May 1988).

[5] D. Véron, Opt. Commun. **10**, 95(1974).

[6] J. P. Crenn, IEEE, MTT-27, **6**, 573(1979).

[7] A. Gondhalekar, P. Lomas, P. Noll, K. Reed and F. C. Schüller, Proceedings 13th Symposium on Fusion Technology (SOFT) Varese, Italy, 24-28 September 1984, CEC Vol. 2, p. 1661 and JET-P(85)01, (1985).

[8] J. A. Fessey, C. W. Gowers, C. A. J. Hugenholtz and K. Slavin, J. Phys. E. Sci. Instrum. **20**, (1987)

[9] J. H. Williamson and D E Evans, IEEE Trans. Plasma Science, **PS-10**, 82(1982).

[10] H. Soltwisch, Course and Workshop on Basic and Advanced Diagnostic Techniques for Fusion Plasmas, Vareena, Sept 1986, CEC Brussels, EUR10797EN, **Vol.II**, 343(1987).

[11] J. Blum, J. Ch. Gilbert and B. Thooris, JET Contract JT3/9008.

[12] H. Salzmann, J. Bundgaard, A. Gadd, C. Gowers, K. B. Hansenk et al., Rev. Sci. Instrum. **59**, 1451(1988).

[13] R. Granetz and P. Smeulders, Nuclear Fusion **28**, 457(1988).